A semi-analytical algorithm for deriving the particle size distribution slope of turbid inland water based on OLCI data: a case study in Lake Hongze

Shaohua Lei [a, b], Jie Xu [a], Yunmei Li [a, *], Lin Li [b], Heng Lyu [a], Ge Liu [c],

Yu Chen [d], Chunyan Lu [e], Chao Tian [b], Wenzhe Jiao [b]

[a] Jiangsu Center for Collaborative Innovation in Geographical Information Resource Development and Application, Key Laboratory of Virtual Geographical Environment of Ministry of Education, School of Geography, Nanjing Normal University, Nanjing 210023, China;

[b] Department of Earth Sciences, Indiana University-Purdue University Indianapolis (IUPUI), IN 46202, USA

[c] Northeast Institute of Geography and Agricultural Ecology, Chinese Academy of Sciences, Changchun 130102, China;

[d] Key Laboratory of Digital Earth Science, Institute of Remote Sensing and Digital Earth, Chinese Academy of Sciences, Beijing 100094, China;

[e] College of Computer and Information Sciences, Fujian Agriculture and Forestry University, Fuzhou 350002, China;

* Corresponding author: Jiangsu Center for Collaborative Innovation in Geographical Information Resource Development and Application, Key Laboratory of Virtual Geographical Environment of Ministry of Education, School of Geography, Nanjing Normal University, Nanjing 210023, China (Y. Li)

E-mail addresses: liyunmei@njnu.edu.cn (Y. Li)

A semi-analytical algorithm for deriving the particle size distribution slope of turbid inland water based on OLCI data: a case study in Lake Hongze

ABSTRACT: The particle size distribution (PSD) slope (ξ) can indicate the predominant particle size, material composition, and inherent optical properties (IOPs) of inland waters. However, few semi-analytical methods have been proposed for deriving ξ from the surface remote sensing reflectance due to the variable optical state of inland waters. A semi-analytical algorithm was developed for inland waters having a wide range of turbidity and ξ in this study. Application of the proposed model to Ocean and Land Color Instrument (OLCI) imagery of the water body resulted in several important observations: (1) the proposed algorithm (754 nm and 779 nm combination) was capable of retrieving ξ with R^2 being 0.72 ($p < 0.01$, n = 60), and MAPE and RMSE being 4.37% and 0.22 (n = 30) respectively; (2) the ξ in HZL was lower in summer than other seasons during the period considered, this variation was driven by the phenological cycle of algae and the runoff caused by rainfall; (3) the band optimization proposed in this study is important for calculating the particle backscattering slope (η) and deriving ξ because it is feasible for both algae dominant and sediment governed turbid inland lakes. These observations help improve our understanding of the relationship between IOPs and ξ, which is affected by different bio-optic processes and algal phenology in the lake environment.

Main finding of this work:

A new semi-analytical PSD slope estimation algorithm suitable for algae or sediment dominant water was developed.

Keywords: PSD slope; Back scattering slope; Turbid inland waters; OLCI; Lake Hongze

1. Introduction

The size distribution range of organic phytoplankton communities and inorganic particles in lake environments is different due to the difference of particle type, internal structure, and shape (Stramski et al., 2004; Vaillancourt et al., 2004). Therefore, particle size distribution (PSD) characteristics are important indicators of biogeochemical cycling and can be monitored optically because they are the major sources of backscattering (Hovenier, 2000; Risović, 2002; Stramski and Mobley, 1997). The slope (denoted as ξ) of PSD is the value of exponential position when the number concentration of suspended particulate matter (SPM) in water is fitted by a Junge-type (Junge, 1963) power law function (Boss et al., 2001; Stramski and Kiefer, 1991). The ξ is usually informative for understanding the contribution of SPM to the flocculation, transport, deposition, and carbon cycle in lakes because it is indicative of the relative proportion of small to large SPM in water directly (Garcia Bravo et al., 2011; Tamigneaux et al., 1999; Wedd et al., 2019; Xi et al., 2014). The larger the ξ, the more number concentration of fine inorganic suspended particles (clay and fine silt); the smaller the ξ, the more algae and other organic matter (Neukermans et al., 2012; Stramski et al., 2004). Meanwhile, the ξ value and its changes in time can indirectly reveal the composition of SPM 1(Bader, 1970; Koestner et al., 2019; Reynolds and Stramski, 2019; Sheldon et al., 1972). Furthermore, the inherent optical properties (IOPs) of a compositional diverse SPM is strongly relevant to ξ. A large magnitude ξ magnifies the backscattering of light underwater and plays an important role in driving remote sensing signals (Boss and Pegau, 2001; Boss et al., 2009; Lei et al., 2020b; Loisel et al., 2006; Thosteson and Hanes, 1998; Wozniak et al., 2018). This relevance of ξ to the water IOPs forms the physical basis of using remote sensing to reveal the ξ of SPM in ocean and inland waters (Baker and Lavelle, 1984; Bao et al., 2018; Lamont et al., 2018; Mie, 1908; Thorne and Hurther, 2014).

Two remote sensing models have been used to map the ξ of SPM. The lookup table (LUT) model was proposed to derive ξ from the slope of particle backscattering coefficient (η) using the Mie theory and was successfully applied to algae dominated global ocean water (Kostadinov et al., 2009). Given the compositional complexity of SPM in inland waters, it is difficult for an LUT model to accommodate the SPM optical properties exhaustively (Evers-King et al., 2017; Li et al., 2018; Reynolds et al., 2016; Song et al., 2017). For example, the complex refraction index of a particle assemblage can vary as the phytoplankton species or mineral composition changes, thus an LUT model constructed for one lake may not be suitable for other lakes (Huang et al., 2014;

Mishra et al., 2005; Stramski, 1999). Also, an LUT model does not have an explicit relationship (Arabsahebi et al., 2020; Bowden and Taylor, 2019; Hu et al., 2012; Ogashawara et al., 2016). Additionally, an empirical model was proposed by Lei et al. (2019b) to describe the relationship between the ratio of remote sensing reflectance red band R_{rs}(Red) to green band R_{rs}(Green) and ξ for Lake Hongze. Despite its robust performance in characterizing the correlation of ξ to the apparent optical properties (AOPs) via regression analysis, the empirical method lacks a mechanistic explanation for the resultant relationship (Li et al., 2017; Sun et al., 2019). On the contrary, the semi-analytical method has an advantage over the empirical method of offering a rational explanation on the relationship of SPM IOPs and ξ, and is often a favorable approach to assess the quality of inland waters with remote sensing (Oyama et al., 2009; Watanabe et al., 2016; Werdell et al., 2018). However, few studies have been devoted to the development of semi-analytical methods for determining the ξ of inland lakes.

Establishment of a strong performing semi-analytical algorithm is required considering the complexity of SPM in inland lakes as well as the variation of the corresponding IOPs (Grunert et al., 2019; Peng and Effler, 2012). Algae dominated turbid inland water is expected to show a small magnitude ξ (Koestner et al., 2019; Kostadinov et al., 2012; Lei et al., 2019a; Qi et al., 2018). Furthermore, the IOPs of algal particles can vary with algal species, physiological adaptations, and morphology due to the ratio of chlorophyll to cellular carbon changes (Behrenfeld et al., 2005; Kostadinov et al., 2009; Wang et al., 2016; Xu et al., 2019b; Zhang et al., 2019a). In contrast, a water body can exhibit a larger magnitude ξ due to the dominance of inorganic particles such as clay and fine silt (< 6 μm) due to river discharge into the lake and/or wind disturbed resuspension from the lake bottom. (Bowers and Binding, 2006; Chen et al., 2015; Lei et al., 2020a; Li et al., 2015; Xu et al., 2019c; Zhang et al., 2019b). In other words, the efficiency of the backscattering of organic matter is usually low, while typical inorganic minerals present strong backscattering (Serra et al., 2001; Zhang et al., 2010). This fundamental IOP difference between the sediment governed water and the algae dominated water results from the compositional nature of SPM in these two types of inland waters (Du et al., 2018; Halse and Syvertsen, 1996; Qi et al., 2018; Wang et al., 2019; Xu et al., 2018; Xu et al., 2019a; Yu, 2019). Therefore, understanding and exploring the relationship between the SPM IOPs and ξ of inland lakes is the premise to establish a reliable semi-analytical algorithm and is worthy of more research (Huang et al., 2016; Sun et al., 2017).

Lake Hongze (HZL) is the fourth largest freshwater lake in China and provides drinking water for about 5 million people of Huaian City. Suspended sediments are the main particulate matter of HZL due to the inflow of the Huai River (Cao et al., 2018). In recent years, algal blooms occasionally occur in HZL in summer due to rich nutrients in the lake. Hence, operational monitoring of the ξ in this lake is of special significance to the protection of this drinking water resource (Zhao et al., 2014). However, the presence of both sediment and algal particulates results in complex optical properties (Li et al., 2019b; Xiong et al., 2019), the ξ can be affected by the stream discharge, temperature-driven algal phenology, and local hydrodynamic conditions such as wind-driven current (Lyu et al., 2017; Maeda et al., 2019; Peng et al., 2019). Although an empirical model was previously proposed to retrieve ξ in HZL (Lei et al., 2019b) from the AOPs of the lake, a thorough understanding of the relationship between SPM IOPs and ξ was missing.

The main objective of this research is to develop a semi-analytical algorithm for estimating ξ with SPM IOPs. With abundant spectral bands, the Sentinel 3A/OLCI (Ocean and Land Color Instrument) imagery provides great potential for remotely monitoring coastal and inland waters, thus OLCI images were used to construct the semi-analytical model for estimating ξ in HZL. The specific objectives are to determine (1) the optimal band combination of OLCI to describe the relationship between the η and ξ in inland lakes, (2) the spatiotemporal distribution of the ξ of HZL, and (3) the transferability of the proposed semi-analytical algorithm. To our knowledge, this is the first study to employ Sentinel 3A/OLCI images to quantitatively estimate ξ using a semi-analytical method in inland lakes.

2 Materials and methods

2.1 Study area

Lake Hongze (HZL) is a shallow lake (the average water depth is 1.9 m) with a latitude between 33°06′ N and 33°40′ N and longitude between 118°10′ E and 118°52′ E. HZL is an artificial dammed lake and is connected with the Huai River, shown in figure 1. The main discharge entering HZL is Huai River which makes up over 70 percent of total runoff entering into HZL (Lei et al., 2019a; Tang, 2007).
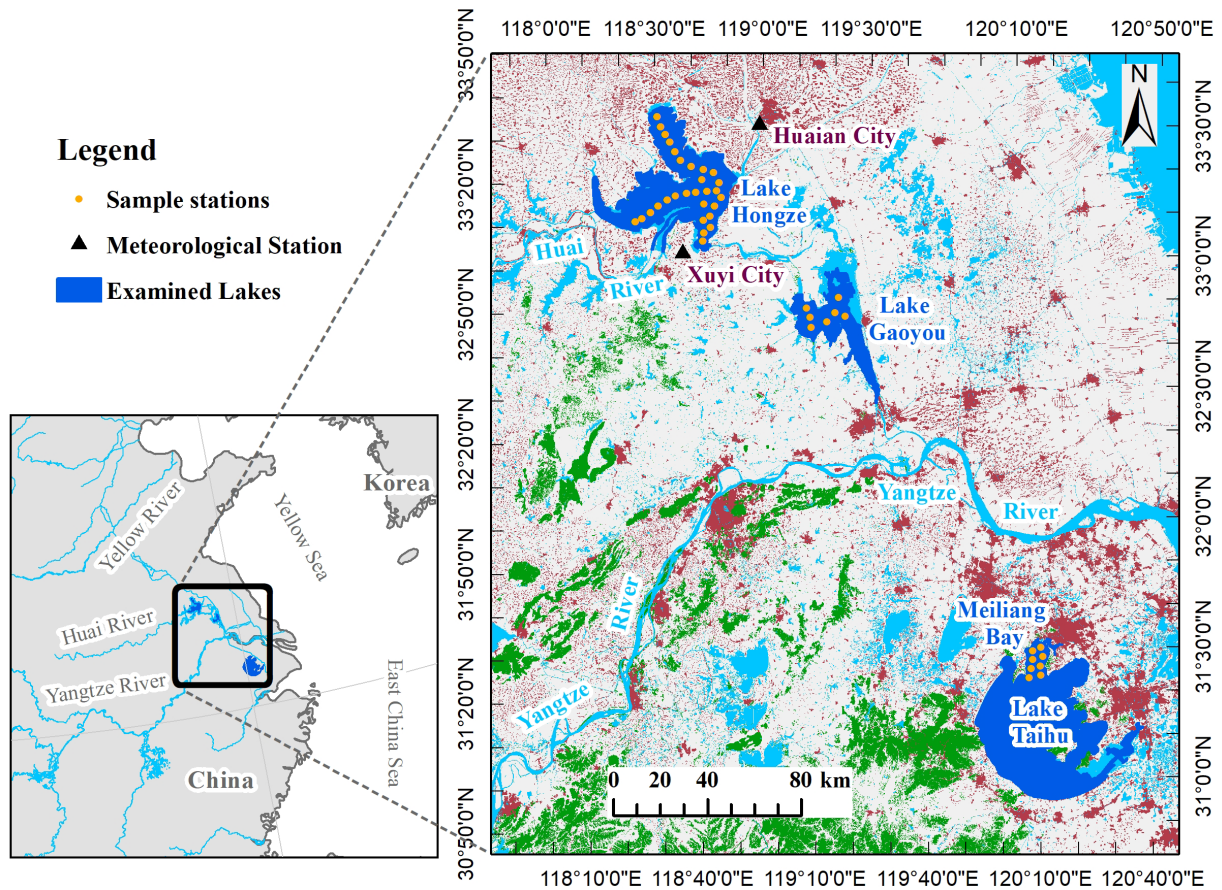
Figure 1. Location of three examined lakes (in dark blue colour) Lake Hongze, Lake Gaoyou, and Lake Taihu in China. The yellow points in the three lakes represent the location of in situ experiments. The black triangle near Lake Hongze represents the meteorology stations (Huaian No.58141 and Xuyi No.58138). The shallow blue colour represents the rivers and water bodies. The red colour represents construction land and the green colour represents forest land.

2.2 Field data collection

Figure 1 shows the location of the *in situ* measurements performed in the three highly turbid inland waters: HZL, Lake Gaoyou, and Lake Taihu.

From 2016 to 2018, four *in situ* experiments were conducted in HZL. Remote sensing reflectance $R_{rs}(\lambda)$ (Mueller et al., 2003) and PSD data were collected at the same time from 90 sampling points. The PSD and corresponding water samples were obtained from a 20 cm water depth underwater. Water samples were analyzed in the laboratory to determine the mass concentrations of SPM (CSPM) gravimetrically (Zhang et al., 2007) and chlorophyll *a* (Chl*a*) fluorometrically (Welschmeyer, 1994), respectively. The PSD data were measured using a LISST-100X instrument calibrated with MilliQ water before data collection was performed (Lei et al., 2019b). The instrument capable of measuring

particle size ranging from 1.25 to 250 μm (type B, Sequoia, USA) ([Jong and Grant, 2007](#)).
The $N`(D)$ ($m^{-3} \cdot \mu m^{-1}$) is the differential distribution per unit size ([Reynolds et al., 2010](#)):

$$N`(D) = \frac{\frac{6V(D)}{\pi D^3}}{\Delta D} \qquad (1)$$

where D (μm) represents the midpoint of each ring of LISST-100X, the $V(D)$ (μL ·
L^{-1}) represents the volume concentration of the corresponding 32 rings. ΔD represents the
width of each measured size interval. In this study, a power law function was applied to
the PSD ([Bader, 1970](#); [Jonasz and Fournier, 2007](#); [Reynolds et al., 2010](#)):

$$N`(D) = N`(D_0) \left(\frac{D}{D_0}\right)^{-\xi} \qquad (2)$$

where D_0 is 19.2 μm, and the midpoint of the whole logarithmic size ranges from
1.25 to 250 μm ([Lei et al., 2020b](#)). The exponent (ξ) is the slope of the distribution for the
generalized model of particle size distribution.

At the same time, the particle backscattering coefficient at wavelength 852 nm, i.e.,
$b_{bp}(852)$, was measured by the HS-6 ([HOBI Laboratories, 2012](#); [Maffione and Dana,
1997](#)) at a 20 cm water depth underwater. In this study, 60 *in situ* $b_{bp}(852)$ data were used
to validate the accuracy of the η retrieval algorithm.

Field measurements were also made in Lake Gaoyou at 7 sampling points ~~pairs~~ in
September 2018, and in Meiliang Bay of Lake Taihu at 22 sampling points ~~pairs~~ in July
2016 and July 2017. The data measured in Lake Taihu and Lake Gaoyou, the third and
the sixth largest freshwater lakes in China, were used to test the transferability of the
optimal model established with the data for Lake Hongze. The optical characteristics are
different between these two lakes. Lake Gaoyou is a downstream lake to HZL and is
dominated by suspended sediment like HZL. The Meiliang Bay of Lake Taihu is a water
body dominated by algae and frequently experiences algal blooms ([Huang et al., 2019](#)).

2.3 Meteorological data

The monthly precipitation, air temperature, and wind speed data were obtained from
Huaian City (No.58141) and Xuyi City (No.58138) meteorological stations, shown in
Figure 1. The meteorological data are downloaded from the China Meteorological Data
Sharing Service System (http://cdc.cma.gov.cn/) ([Mu et al., 2019](#)).

2.4 Sentinel 3A/OLCI data

A total of 338 cloud-free Sentinel 3A/OLCI Level-0 images of HZL acquired from June 2016 to July 2019 (shown in Table S2) were pre-processed by SeaWiFS Data Analysis System (SeaDAS 7.5.3). To eliminate or weaken the influence of the atmosphere, the Management Unit Mathematical Model (MUMM) was used to perform atmospheric correction (Ruddick et al., 2000). In the MUMM method, the $R_{rs}(779)$ and $R_{rs}(865)$ are used to replace the zero values for water-leaving radiance in the red and near-infrared bands in Gordon's standard atmospheric correction algorithm (Gordon, 1997; Miao et al., 2019).

Among the four data-gathering expeditions conducted in HZL from 2016 to 2018, a total of 46 matching spectra for which the sampling time was close to the OLCI imaging (±3 hour) were chosen to validate the accuracy of the MUMM-derived $R_{rs}(\lambda)$. Furthermore, the complex atmospheric environment over inland lakes makes it difficult to reduce the atmosphere effect perfectly, thus quasi synchronous measured data were used to perform necessary systematic correction.

2.5 Algorithm development and accuracy assessment

2.5.1 Estimating ξ from simulated OLCI $R_{rs}(NIR)$

The subsurface remote sensing reflectance, $r_{rs}(\lambda)$ (sr^{-1}), can be derived from the above-surface remote sensing reflectance $R_{rs}(\lambda)$ (Gordon, 1988).

$$r_{rs}(\lambda) = \frac{R_{rs}(\lambda)}{0.52 + 1.7R_{rs}(\lambda)} \tag{3}$$

According to Lee et al. (1998) and Gordon (1988), $r_{rs}(\lambda)$ can be defined by the total absorption $a(\lambda)$ (m^{-1}) and backscattering $b_{b}(\lambda)$ (m^{-1}) coefficients:

$$\frac{\left(-g_0 + [g_0{}^2 + 4 * g_1 * r_{rs}(\lambda)]^{\frac{1}{2}}\right)}{2g_1} = \frac{b_{b}(\lambda)}{[a(\lambda) + b_{b}(\lambda)]} \tag{4}$$

In higher-scattering coastal waters, g_0 and g_1 are wavelength-independent constants 0.084 and 0.17. The parameters $b_{b}(\lambda)$ and $a(\lambda)$ are IOPs of different water component:

$$b_{b}(\lambda) = b_{bp}(\lambda) + b_{bw}(\lambda) \tag{5}$$

$$a(\lambda) = a_{ph}(\lambda) + a_{nap}(\lambda) + a_{w}(\lambda) + a_{CDOM}(\lambda) \tag{6}$$

The absorption and backscattering coefficients of pure water ($a_{w}(\lambda)$ and $b_{bw}(\lambda)$) are known (Pope and Fry, 1997). When λ is between 700 nm and 900 nm, the absorption

coefficients of total suspended particulate matter, $a_{\text{p}}(\text{NIR})$ (including absorption coefficients of pigment particles ($a_{\text{ph}}(\text{NIR})$) and non-pigmented particulate matter ($a_{\text{nap}}(\text{NIR})$)), and coloured dissolved organic matter ($a_{\text{CDOM}}(\text{NIR})$) can be ignored in the near-infrared (Shi et al., 2019a; Shi and Wang, 2019; Sun et al., 2016). Thus, $b_{\text{bp}}(\text{NIR})$ can be obtained. Subsequently, η can be derived by any two bands λ_0 and λ_1 in the NIR as shown below:

$$b_{\text{bp}}(\lambda_1) = b_{\text{bp}}(\lambda_0) * \left[\frac{\lambda_1}{\lambda_0}\right]^{-\eta} \tag{7}$$

$$\eta = -\frac{\ln\left(\frac{b_{\text{bp}}(\lambda_1)}{b_{\text{bp}}(\lambda_0)}\right)}{\ln\left(\frac{\lambda_1}{\lambda_0}\right)} \tag{8}$$

Finally, the slope of PSD mentioned in equation (2) is derived based on the relationship between the slope of the backscattering coefficient η and ξ.

2.5.2 Performance matrix

The performance of the various developed band combination algorithms was assessed by IBM SPSS (Statistical Product and Service Solutions) 17 with mean absolute percentage error (MAPE) and root mean square error (RMSE):

$$\text{MAPE} = \frac{1}{n}\sum_{i=1}^{n}\left|\frac{X_{obs,i} - X_{model,i}}{X_{obs,i}}\right| * 100\% \tag{9}$$

$$\text{RMSE} = \sqrt{\frac{\sum_{i=1}^{n}(X_{obs,i} - X_{model,i})^2}{n}} \tag{10}$$

where n is the number of training or testing samples, and X_{obs} and X_{model} represent the *in situ* and predicted values for samples, respectively.

3 Results

3.1 Water constituent concentrations

Table S1 shows the concentrations of water components in HZL. CSPM ranged from 7.82 mg l^{-1} to 100.00 mg l^{-1} with a mean value of 49.37 ± 23.85 mg l^{-1}. Chl*a* was at a lower level (12.10 ± 10.75 µg l^{-1}). Due to the phenology of phytoplankton, Chl*a* in winter was lower than that in summer, decreasing from 22.02 ± 19.87 µg l^{-1} in July 2016 to 9.83

± 4.95 µg l^{-1} in December 2016 as a result of an increasing trend of inorganic substances. The dominance of inorganic SPM in the turbid water led to a high ξ (3.92 $\pm$ 0.34) and $b_{\mathrm{bp}}(852)$ (0.76 $\pm$ 0.36 m^{-1}) (Zeng et al., 2020).

3.2 In situ spectra-based ξ model

In this study, a total of 90 *in situ* ξ measurements and $R_{\mathrm{rs}}(\lambda)$ data were used to develop the Sentinel 3A/OLCI-based ξ retrieval model with 2/3 sample points (60 points) being randomly selected for calibration and the rest (30 points) for validation. The *in situ* $R_{\mathrm{rs}}(\mathrm{NIR})$ are used to simulate the bands of OLCI (700–900 nm) using relative spectral response function (SRF). Seven near-infrared OLCI bands (Donlon et al., 2012; Jorge et al., 2017), named Oa11/12/13/16/17/18/19 (note that the O$_2$ absorption bands of Oa14/15 were not selected here) were used to derive $b_{\mathrm{bp}}(\mathrm{NIR})$ using equations (3)-(8).

Twenty one NIR band combinations of the simulated OLCI spectra were tested for their performance for the retrieval of η. Table 1 shows that the No.3 NIR band combination resulted in the highest correlation coefficient (R = 0.85) between the *in situ* and simulated $b_{\mathrm{bp}}(852)$. However, the corresponding MAPE and RMSE of $b_{\mathrm{bp}}(852)$ are higher than those for No.8 combination, indicating the superior performance of the latter to the former. Correspondingly, the same band combinations were compared for their performance for establishing the ξ model. The resultant correlation coefficient, R ranges from -0.34 to 0.85 for the calibration and from -0.19 to 0.79 for the validation, implies that not all of the NIR bands are suitable for deriving ξ. It is clear that the No. 8 combination (754 nm of Oa12 and 779 nm of Oa16 band pair) resulted in the highest R (R = 0.85) in the calibration and the lowest MAPE (4.37%) and RMSE (0.22) in the validation (Figure 2 (a)).

Table 1 Results from using various NIR bands for developing the relationship between η and ξ using *in situ* data. The bold font indicates the best combination used in this study.

Combinations of λ(NIR)			Model validation of $b_{\mathrm{bp}}(852)$, n=60					Model (η vs. ξ), n=60			Model validation of ξ, n=30				
No.	λ_1	λ_0	r	Slope	Intercept	MAPE	RMSE	r	Slope	Intercept	r	Slope	Intercept	MAPE	RMSE
1	754	709	0.82	3.88	-0.32	258.58	2.35	-0.34	-0.05	3.52	0.23	0.08	3.59	7.20	0.35
2	762	709	0.82	2.89	-0.16	179.92	1.62	-0.31	-0.05	3.58	0.28	0.09	3.55	7.13	0.34
3	779	709	0.85	1.67	0.12	98.26	0.77	-0.17	-0.04	3.72	0.10	0.02	3.84	7.46	0.36

4	865	709	0.79	0.88	0.22	46.03	0.28	-0.24	-0.07	3.73	0.16	0.04	3.72	7.45	0.36
5	885	709	0.74	0.81	0.25	48.25	0.29	-0.18	-0.05	3.78	0.17	0.04	3.76	7.51	0.35
6	900	709	0.74	0.77	0.28	48.88	0.29	-0.19	-0.06	3.75	0.20	0.05	3.70	7.88	0.37
7	762	754	0.55	0.97	0.20	56.44	0.56	0.10	0.01	3.89	-0.06	0.00	3.91	8.11	0.37
8	**779**	**754**	**0.83**	**0.74**	**0.22**	**31.23**	**0.20**	**0.85**	**0.29**	**3.56**	**0.79**	**0.62**	**1.47**	**4.37**	**0.22**
9	865	754	0.79	0.93	0.22	48.58	0.31	-0.06	-0.02	3.89	0.06	0.00	3.87	7.72	0.36
10	885	754	0.76	0.92	0.24	53.82	0.35	-0.01	0.00	3.90	0.08	0.00	3.90	7.73	0.36
11	900	754	0.76	0.92	0.27	55.64	0.36	0.00	0.00	3.90	0.14	0.00	3.90	7.73	0.36
12	779	762	0.70	0.67	0.27	39.34	0.27	0.48	0.07	3.81	0.53	0.27	2.85	7.28	0.35
13	865	762	0.79	0.93	0.22	48.29	0.31	-0.09	-0.03	3.89	0.00	0.00	3.89	7.70	0.36
14	885	762	0.76	0.93	0.24	53.09	0.34	-0.04	-0.01	3.90	0.05	0.00	3.89	7.72	0.36
15	900	762	0.76	0.92	0.26	54.66	0.35	-0.03	-0.01	3.89	0.11	0.00	3.88	7.81	0.36
16	865	779	0.79	0.92	0.22	47.69	0.30	-0.26	-0.07	3.85	0.19	0.06	3.63	7.64	0.36
17	885	779	0.76	0.91	0.24	51.40	0.33	-0.17	-0.04	3.87	0.18	0.03	3.78	7.62	0.35
18	900	779	0.77	0.90	0.26	52.26	0.33	-0.16	-0.04	3.85	0.23	0.05	3.71	8.03	0.38
19	885	865	0.78	0.89	0.23	52.36	0.31	0.07	0.00	3.91	-0.16	-0.01	3.92	7.82	0.36
20	900	865	0.78	0.91	0.21	50.28	0.30	0.06	0.00	3.91	-0.19	-0.01	3.93	8.04	0.37
21	900	885	0.52	0.89	0.28	70.21	0.57	-0.02	0.00	3.89	0.07	0.00	3.89	7.80	0.36

3.3 Application of the model to synchronizing images

When compared with the 46 (see Section 2.4) *in situ* simulated $R_{rs}(\lambda)$ and the quasi-synchronous OLCI $R_{rs}(\lambda)$ after atmospheric correction (AC) for bands 754 nm and 779 nm (Figure 2 (b) and (c)), the MUMM-derived $R_{rs}(\lambda)$ was systematically lower though the R^2 is 0.78 and 0.74, respectively. This means that the MUMM-derived $R_{rs}(\lambda)$ should be recalibrated against the *in situ* measurements before being applied to the OLCI images.

$$R_{rs}(754)_{in\,situ} = 2.0058 * R_{rs}(754)_{MUMM} - 0.0091 \qquad (11)$$

$$R_{rs}(779)_{in\,situ} = 1.8515 * R_{rs}(779)_{MUMM} - 0.0073 \qquad (12)$$

After using equations (11) and (12) for the systematic conversion, the MAPE was reduced from 24.28% to 15.93% for band 754 nm, and from 24.84% to 16.74% for band 779 nm, the RMSE was reduced to 0.003 Sr^{-1}. As shown in Figure 2 (d), the use of the recalibrated OLCI spectra led to more accurate ξ estimates with MAPE, RMSE, and R^2 being 4.87%, 0.24, and 0.73, respectively.
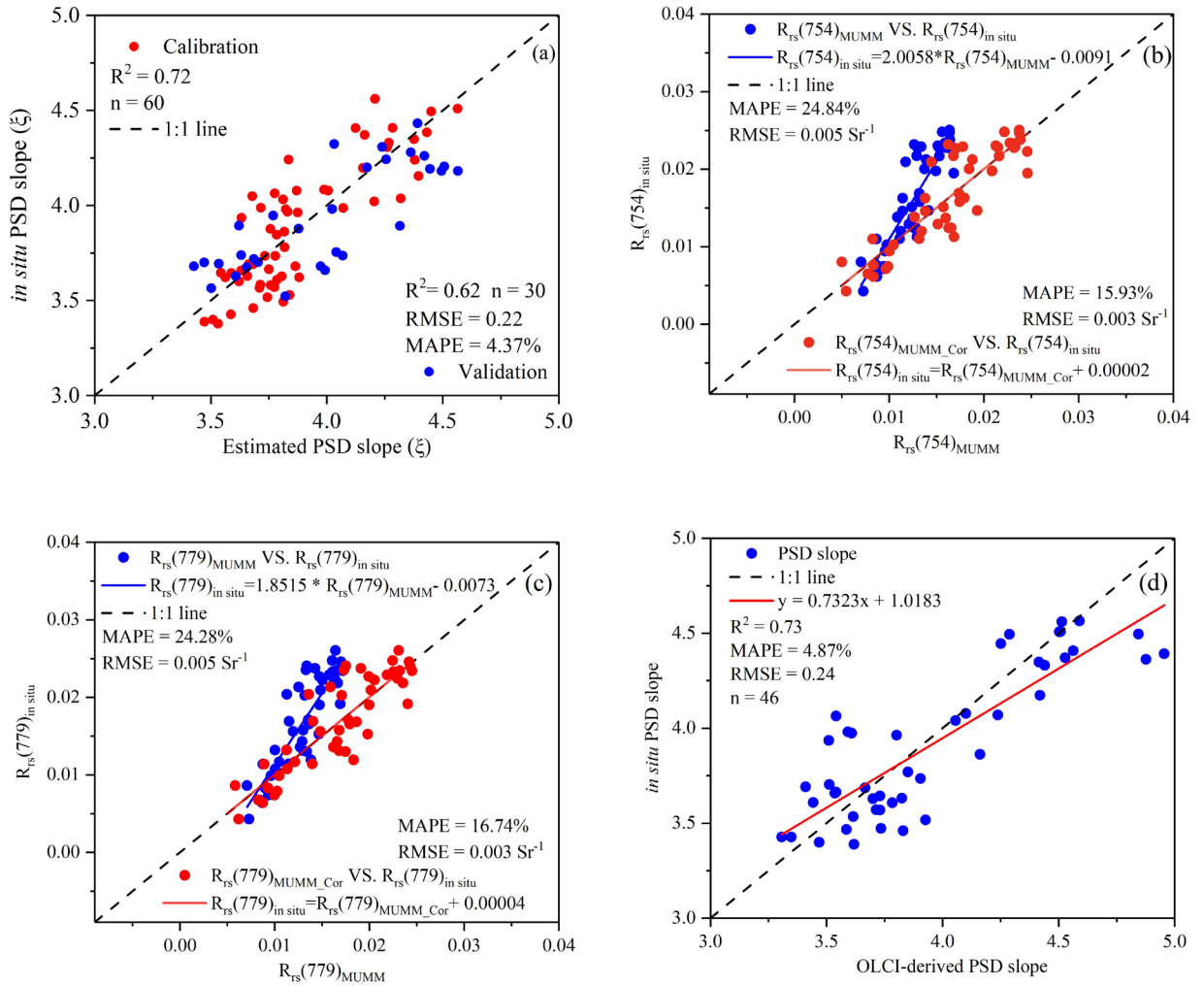
Figure 2. (a) Calibration and validation of the algorithm for estimating the ξ from η. Validation scatters diagram of OLCI products of (b) $R_{rs}(754)$, (c) $R_{rs}(779)$, and (d) the ξ comparing with the *in situ* data in ±3 hour difference from imaging. $R_{rs}(754)_{MUMM-Cor}$ and $R_{rs}(779)_{MUMM-Cor}$ represent the corrected R_{rs} using the formula (11) and (12).

3.4 Applicability of the model to in situ data of other lakes

The ξ retrieval algorithm established for HZL was also tested with the *in situ* data measured in Lake Gaoyou and Lake Taihu. Overall, testing the transferability of the ξ algorithm resulted in a systematic bias ($R^2 = 0.62$, RMSE = 0.26, MAPE = 6.42%, n = 29) when applied to 29 samples collected from both Lake Gaoyou and Lake Taihu. When 29 samples were stratified for the test, the model performed differently. For Lake Gaoyou, despite a little underestimation, the algorithm performed satisfactorily with the RMSE and MAPE being 0.13 and 3.13% (n = 7, Figure 3), respectively. This strong model performance may be attributed to the geographical location and the similarity of the optical properties of Lake Gaoyou to those of HZL.

However, the performance of the proposed algorithm was found to be low when applied to the data collected for Lake Taihu (RMSE is 0.29 and MAPE is 7.47%, Figure 3). The trend line between the estimated and *in situ* ξ is below the 1:1 line. When the coefficient of determination is high, a slope of one and a zero intercept are necessary to indicate a strong correlation. Although the R^2 and slope are very satisfactory (y = 1.0348x - 0.3999, R^2 = 0.81, n = 22), the intercept is high, almost 0.4. After a systematic correction using the above formula in Lake Taihu, the performance of the algorithm was improved significantly (RMSE = 0.10 and MAPE = 2.18%).
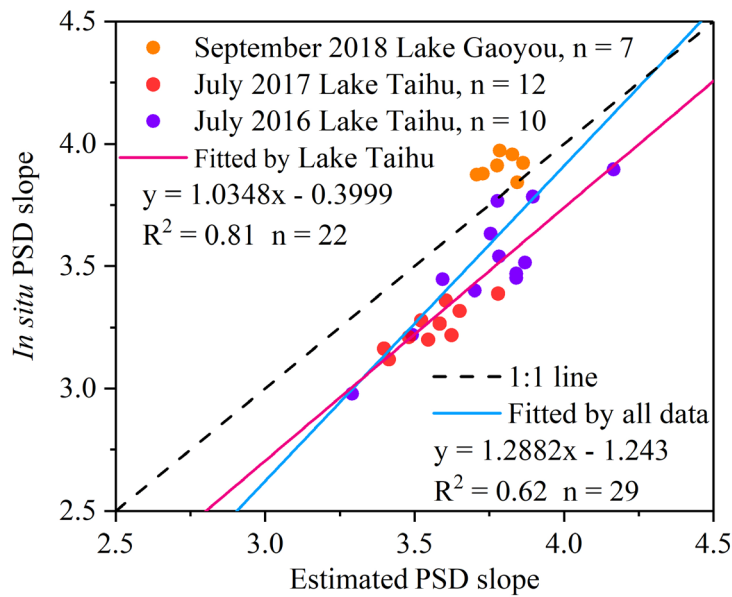
Figure 3: Scatter plot between the estimated and *in situ* ξ in Lake Taihu and Lake Gaoyou.

3.5 Spatiotemporal variability of ξ in HZL

3.5.1 Spatial variability of OLCI-derived ξ in HZL

Spatially, in Figure 4 (a), HZL shows higher ξ values in the middle and east of the lake and lower near the shore, especially the western bay of the lake. The average ξ of HZL was 3.79 ± 0.41.
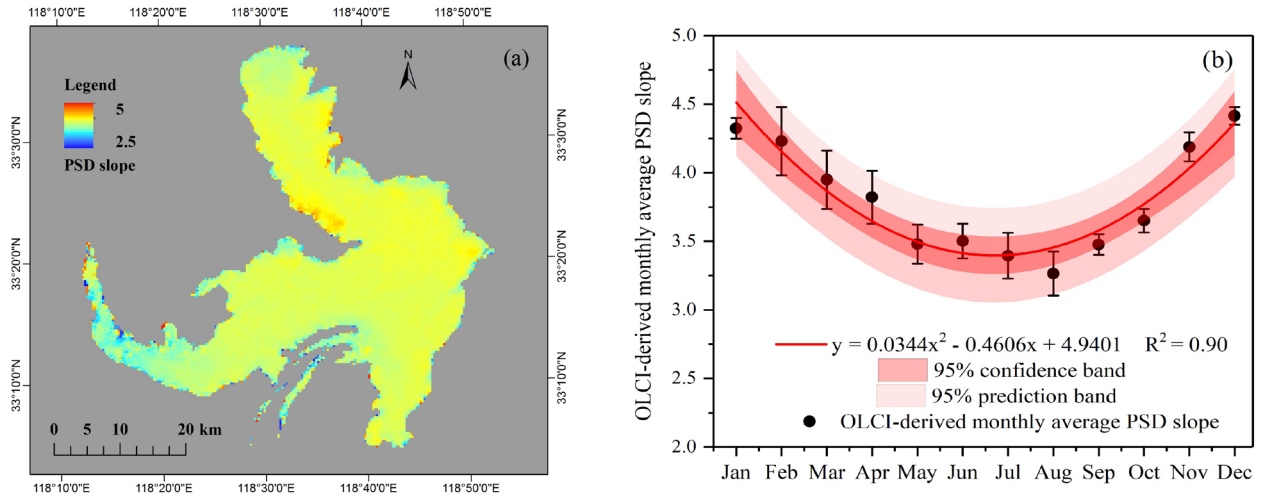
Figure 4: (a) Spatial and (b) monthly average distribution of ξ from June 2016 to July 2019 in HZL.

3.5.2 Temporal variability of OLCI-derived ξ in HZL

Seasonally, the ξ values from HZL were highest in winter (December-February) at 4.32 ± 0.09, moderate in spring and autumn (March-May and September-November) at 3.75 ± 0.24 and 3.77 ± 0.37, and lowest in summer (June-August) at 3.39 ± 0.12. A slightly increasing trend can be observed in Figure 5 and Figure 6 from 2016 to 2019. As shown in Figure 4 (b), Figure 5, and Figure 6, the monthly mean ξ value in HZL can be fitted with a quadratic equation with R^2 being 0.90.
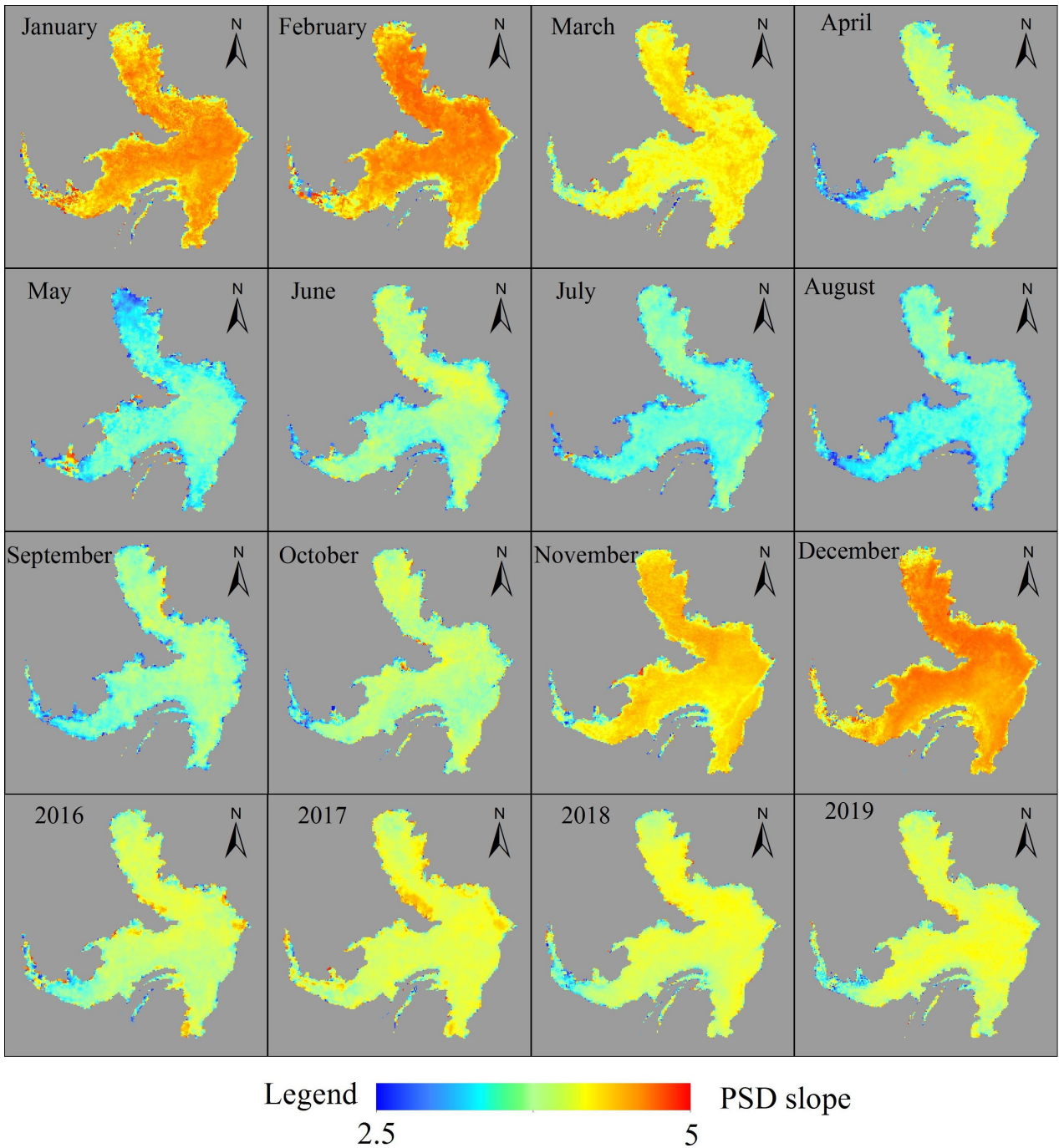
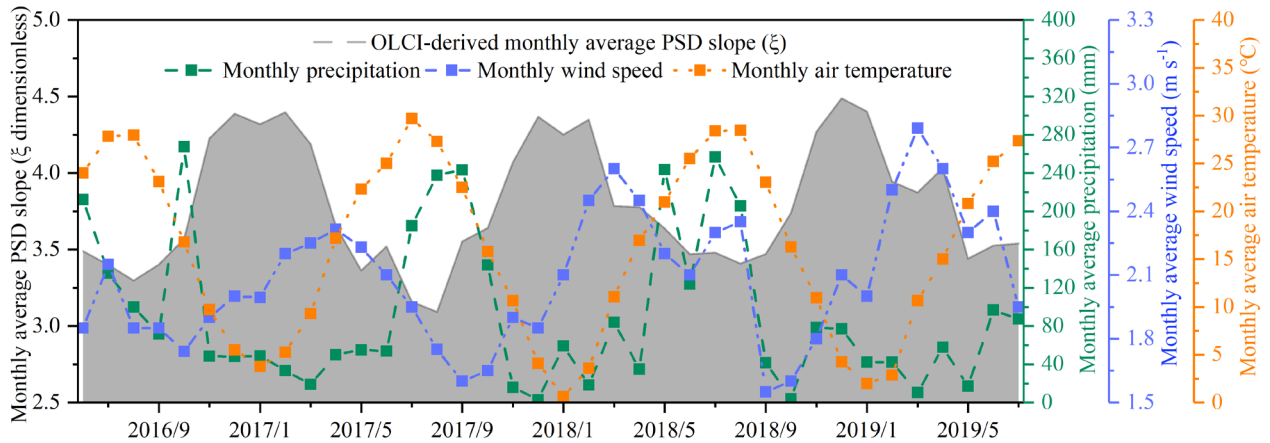Figure 5. Monthly and yearly average spatial distribution of ξ from June 2016 to July 2019 in HZL.

Figure 6: Monthly distribution of OLCI-derived ξ, precipitation, wind speed, and air temperature from June 2016 to July 2019 in HZL. The averaged climate data of the two meteorological stations were used for analysis in this study.

4. Discussion

4.1 Optimal NIR band combinations for relating η to ξ using in situ data

Based on the equations presented in Section 2.5.1, the $R_{rs}(\lambda)$ of sediment dominated turbid waters depends primarily on the absorption of pure water and optical properties of sediments in the spectral region 700 nm to 900 nm (Babin and Stramski, 2002). This is because the $a_p(NIR)$ and $a_{CDOM}(NIR)$ can be ignored, the backscattering of phytoplankton is insignificant, and the $b_{bp}(NIR)$ is much greater than the backscattering of pure water (Shi et al., 2019b; Wu et al., 2011). In theory, the derived η using any two band reflectance values $R_{rs}(NIR)$ should be the same for a given water sample (Xue et al., 2019). However, when a turbid water is rich in algae, the influence of $a_{ph}(709)$ makes the zero $a_{ph}(NIR)$ assumption invalid (Liu et al., 2020). In addition, one absorption peak of O_2 at 761.8 nm may affect $R_{rs}(754)$, $R_{rs}(762)$, $R_{rs}(764)$, and $R_{rs}(768)$, i.e. the OLCI reflectance values at wavelengths 754, 762, 764, and 768 nm, and thus can introduce errors in the derived $b_{bp}(\lambda)$ and η. Studies demonstrate that $R_{rs}(\lambda)$ increases with SPM as exemplified by the presence of the reflectance peak at 820 nm (Li et al., 2019a), which could push the relationship between $b_{bp}(\lambda)$ and η to deviate from the assumed power law decay (Bisson et al., 2019; Lin et al., 2018; Organelli et al., 2018; Thorne and Hurther, 2014), Another possible error source for calculating the $b_{bp}(\lambda)$ and η is a low SNR (signal to noise ratio) of instruments in the near infrared band region such as bands 885 nm and 900 nm because noise can interfere with the derivation of $b_{bp}(\lambda)$ and η from

reflectance. The four error sources mentioned above cause equation (8) to be valid only in some spectral intervals. Therefore, identification of the optimal bands to compute η is essential for the success of this study.

Previous research used a fixed (Shi and Wang, 2019; Sun et al., 2016) band ratio to explore the relationship between η and ξ rather than selecting the optimal one among different band combinations. In this study, an important band optimization framework was proposed to calculate η which was used to derive ξ in turbid inland lakes. Twenty-one NIR band combinations of the simulated OLCI spectra were tested for their performance, but the result shows that not all of the NIR bands combinations are suitable for deriving ξ. Table 1 shows almost 2/3 band combinations present negative correlation coefficients between the η and ξ even though the relationship between the two should be positive according to the Mie theory (Kostadinov et al., 2009; Mie, 1908). Since most of the validation results present high MAPE (> 7%) and RMSE (> 0.35) values, optimization of the band combinations for estimating η is an essential step for accurate prediction of ξ. Otherwise, the model for prediction of ξ could result in unexpected results or inaccurate estimates, as shown by the two examples below.

Shi and Wang (2019) applied the three-order polynomial function between η and ξ proposed by Kostadinov et al. (2009) to calculate ξ using two NIR bands (745 nm and 865 nm) of VIIRS (Visible Infrared Imaging Radiometer Suite) data. However, the VIIRS-derived ξ for the inland lakes considered in Shi and Wang (2019) was not consistent with most previous studies on Lake Taihu (Shi et al., 2018; Xu et al., 2019c; Zhang et al., 2016). For example, given that ξ is positively correlated to the concentration of SPM in inland lakes (Lei et al., 2019b), the spatial pattern of ξ observed by Shi and Wang (2019) was low in the southern part of Lake Taihu where high sediments often govern SPM (Shi et al., 2019b; Shi et al., 2018). Such deviation may result from inappropriate band selection for calculating η in inland lakes.

In addition, in the Bohai Sea and the Yellow Sea, a negative relationship was found between η and ξ by Sun et al. (2016) using the MODIS (Moderate Resolution Imaging Spectroradiometer) bands of 748 nm and 869 nm. However, most of the reported relationships between η and ξ were positive when η ranged from -0.5 to 4 (Huang et al., 2016; Kostadinov et al., 2009; Kostadinov et al., 2012). The negative correlation reported by Sun et al. (2016) between η and ξ may also suggest inappropriate band selection to derive ξ.

4.2 Influence of meteorological factors on the monthly OLCI-derived ξ

External factors, such as river sediment discharge, wind-driven suspension of sediments, and air temperature-driven algal phenology processes could substantially affect ξ, as shown in Figure 6 (Guo et al., 2017; Maeda et al., 2019; Villa et al., 2018). The monthly air temperature, wind speed, and precipitation data from the Huaian City (No.58141) and Xuyi City (No.58138) were analyzed to assess the influence of meteorological factors on ξ, shown in Figure 1. In this study, precipitation data were used as the substitute for river runoff, as the two variables are strongly and positively correlated (Mendes et al., 2017; Zuo et al., 2012).

Figure 7 shows that there is a negative and robust correlation ($p < 0.05$) between monthly average ξ and air temperature of HZL, the coefficient of determination is high (0.81). Meanwhile, the coefficient of determination between monthly ξ and precipitation is high ($R^2 = 0.79$, n = 12, $p < 0.05$). The two strong trends characterizing the influence of air temperature and precipitation on the monthly ξ indicate that suspended algae and solids are greatly influenced by air temperature-driven algal phenology and lake inflows. Meanwhile, there is a positive but very weak correlation between monthly average ξ and wind speed ($R^2 = 0.03$, n = 12, $p > 0.05$). These data are consistent with observations of previous studies (Kondolf et al., 2018; Minghelli et al., 2019; Shi et al., 2015; Watanabe et al., 2018).
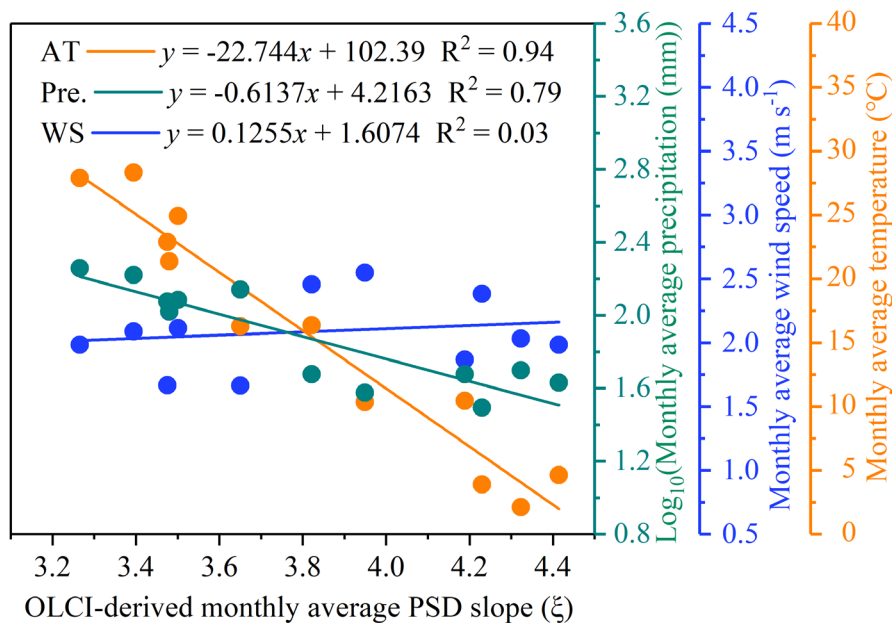

Figure 7: Correlation analysis between the monthly averaged OLCI-derived ξ and monthly averaged precipitation (Pre.), wind speed (WS), air temperature (AT) from June 2016 to July 2019 in HZL.

4.3 Transferability of the algorithm applies to other lakes using in situ data

From the above discussion, the proposed algorithm represents an innovative alternative to deriving ξ in inland lakes. In Section 3.4, the assessment result for Lake Gaoyou is even better than HZL as indicated by lower RMSE and MAPE values of the former compared to the corresponding values of the latter. This algorithm is shown to be effective when applied to other lakes with the same optical properties as HZL. However, the number of *in situ* validation points from Lake Gaoyou is small and the data were collected within a limited sampling time window. Additional data from sediment dominated lakes are required to further test the applicability of the proposed algorithm.

The algorithm was also calibrated on the samples from Meiliang Bay, Lake Taihu where organic algal particles primarily constitute the suspended matter and the particle density and size should be different from those in HZL (Huang et al., 2019; Lyu et al., 2017; Zhang et al., 2019a). However, a high coefficient of determination ($R^2 = 0.81$) was obtained, indicating that the relationship between the slope of particle backscattering η and the PSD slope ξ for Lake Taihu should have a similar linear trend to that of HZL despite different intercepts. Also, the optimal band combination identified for HZL to compute η and ξ is viable for Lake Taihu. The proposed method represents a valuable reference to investigate the η and ξ in the algae dominated water.

Due to the potential effects of particle number concentration, shape, and internal structure, the relationship between η and ξ can vary. Two of the η vs. ξ relationships previously published by others (Figure 8 curve b and d) (Huang et al., 2016; Kostadinov et al., 2012) were compared with the optimal ξ algorithm proposed by this paper (Figure 8 curve a and c). The comparison shows much lower coefficients of determination (< 0.5) for the results reported by others than those by the current study, which can be explained by the use of the optimal band combination in the current study for deriving η.

For Lake Poyang where mineral particles are more common as a result of sediment resuspension and river runoff, the relationship between η and ξ is governed by inorganic particles. The results described in Huang et al. (2016) were based on only 12 observations with a mean CSPM value of 11.05 mg l^{-1}, suggesting that their relationship could be applied to much less turbid waters than HZL with the CSPM being 49.37 ± 23.85 mg l^{-1}. This explains why relationships between η and ξ for the two lakes are very similar but have slightly different slopes as shown in Figure 8 curve a and b. Also, in Figure 8 curve c and d, for Santa Barbara Channel (Kostadinov et al., 2012) and Lake Taihu, different

algal species can have different phytoplankton size populations and should have different relationships between η and ξ. Therefore, the intercept and slope between η and ξ are different from each other. In short, various η vs. ξ relationships in Figure 8 may be attributed to varying component properties in inorganic particle dominated waters and algae particle dominated water in inland lakes (Ahn and Grant, 2007; Babin et al., 2003; Bowers et al., 2009; Qing et al., 2014).
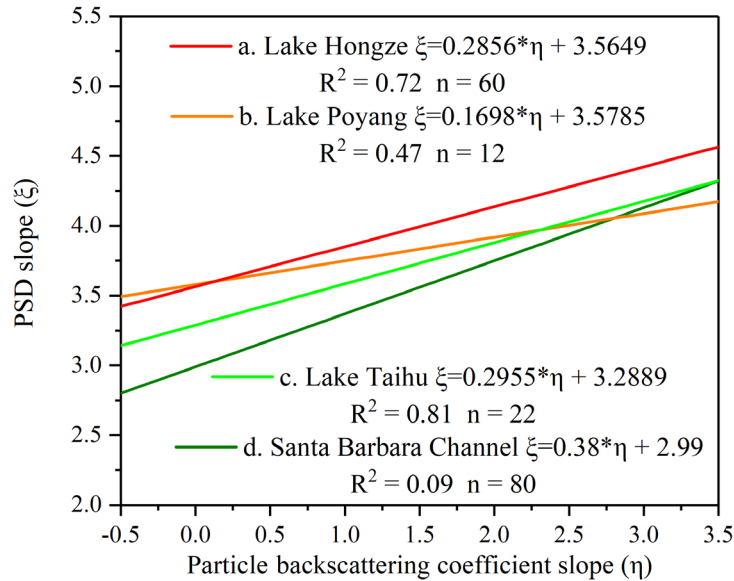

Figure 8. The relationship between η and ξ in different water regions.

5. Conclusions

In this paper, a band optimization semi-analytical method was proposed to calculate the particle backscattering slope (η) from which the PSD slope (ξ) is derived for several turbid inland lakes. Twenty-one NIR band combinations of simulated OLCI spectra were examined for their performance, and bands 754 nm and 779 nm have been identified as the optimal band combination to compute η and ξ for HZL and Lake Gaoyou (inorganic particle dominated waters); this band combination also proved to be viable for Lake Taihu (algae dominated waters). The proposed semi-analytical algorithm resulted in a MAPE of 4.37% and an RMSE of 0.22 for estimating ξ with OLCI images of HZL. Furthermore, testing this model on an independent dataset of Lake Gaoyou proved its satisfactory performance (RMSE = 0.13 and MAPE = 3.13%). The model showed a systematic bias when applied to algae dominated waters, such as Lake Taihu, but a systematic correction

improved the performance of the algorithm significantly (RMSE = 0.10 and MAPE = 2.18%).

HZL showed higher ξ in the eastern lake but lower in the western lake bay from June 2016 to July 2019. On the other hand, the monthly ξ distribution reached high values in winter but low values in summer in HZL, indicating the effects of lake inflows and algal phenology. This finding provides data evidence for managing turbid inland lakes to improve water quality on short and long timescales.

Acknowledgments

Disclosure statement

No potential conflict of interest was reported by the authors.

Funding

References

Ahn, J.H., Grant, S.B., 2007. Size distribution, sources, and seasonality of suspended particles in southern California marine bathing waters. Environ Sci Technol 41, 695-702.

Arabsahebi, R., Voosoghi, B., Tourian, M.J., 2020. A denoising–classification–retracking method to improve spaceborne estimates of the water level–surface–volume relation over the Urmia Lake in Iran. Int J Remote Sens 41, 506-533.

Babin, M., Morel, A., Fournier-Sicre, V., Fell, F., Stramski, D., 2003. Light scattering properties of marine particles in coastal and open ocean waters as related to the particle mass concentration. Limnol Oceanogr 48, 843-859.

Babin, M., Stramski, D., 2002. Light absorption by aquatic particles in the near-infrared

spectral region. Limnol Oceanogr 47, 911-915.

Bader, H., 1970. Hyperbolic distribution of particle sizes. Journal of Geophysical Research 75, 2822-2830.

Baker, E.T., Lavelle, J.W., 1984. Eeffect of particle size on the light attenuation coefficient of natural suspensions. Journal of Geophysical Research 89, 8197-8203.

Bao, W.J., Zhu, S.M., Guo, S.R., Wang, L., Huang, S.X., Fu, J.Y., Ye, Z.Y., 2018. Particle size distribution mathematical models and properties of suspended solids in a typical freshwater pond. Environ Pollut 241, 164-171.

Behrenfeld, M.J., Boss, E., Siegel, D.A., Shea, D.M., 2005. Carbon-based ocean productivity and phytoplankton physiology from space. Global Biogeochem Cy 19, 1-14.

Bisson, K.M., Boss, E., Westberry, T.K., Behrenfeld, M.J., 2019. Evaluating satellite estimates of particulate backscatter in the global open ocean using autonomous profiling floats. Opt Express 27, 30191-30208.

Boss, E., Pegau, W.S., 2001. Relationship of light scattering at an angle in the backward direction to the backscattering coefficient. Appl Optics 40, 5503-5507.

Boss, E., Slade, W., Hill, P., 2009. Effect of particulate aggregation in aquatic environments on the beam attenuation and its utility as a proxy for particulate mass. Opt Express 17, 9408-9420.

Boss, E., Twardowski, M.S., Herring, S., 2001. Shape of the participate beam attenuation spectrum and its inversion to obtain the shape of the particulate size distribution. Appl Optics 40, 4885-4893.

Bowden, S.A., Taylor, C.W., 2019. The application of surface enhanced Raman scattering to the detection of asphaltic petroleum in sediment extracts: Deconvolving three component-mixtures using look-up tables of entire surface enhanced Raman spectra. Anal Methods-Uk 11, 5846-5856.

Bowers, D.G., Binding, C.E., 2006. The optical properties of mineral suspended particles: A review and synthesis. Estuarine, Coastal and Shelf Science 67, 219-230.

Bowers, D.G., Braithwaite, K.M., Nimmo-Smith, W.A.M., Graham, G.W., 2009. Light scattering by particles suspended in the sea: The role of particle size and density. Cont Shelf Res 29, 1748-1755.

Cao, Z., Duan, H., Shen, M., Ma, R., Xue, K., Liu, D., Xiao, Q., 2018. Using VIIRS/NPP and MODIS/Aqua data to provide a continuous record of suspended particulate matter in a highly turbid inland lake. Int J Appl Earth Obs 64, 256-265.

Chen, S., Han, L., Chen, X., Li, D., Sun, L., Li, Y., 2015. Estimating wide range Total Suspended Solids concentrations from MODIS 250-m imageries: An improved method. Isprs J Photogramm 99, 58-69.

Donlon, C., Berruti, B., Buongiorno, A., Ferreira, M.H., Féménias, P., Frerick, J., Goryl, P., Klein, U., Laur, H., Mavrocordatos, C., Nieke, J., Rebhan, H., Seitz, B., Stroede, J., Sciarra, R., 2012. The Global Monitoring for Environment and Security (GMES) Sentinel-3 mission. Remote Sens Environ 120, 37-57.

Du, C.G., Wang, Q., Li, Y.M., Lyu, H., Zhu, L., Zheng, Z.B., Wen, S., Liu, G., Guo, Y.L., 2018. Estimation of total phosphorus concentration using a water classification method in inland water. Int J Appl Earth Obs 71, 29-42.

Evers-King, H., Martinez-Vicente, V., Brewin, B., Dall'Olmo, G., Hickman, A., Jackson, T., Kostadinov, T., Krasemann, H., Loisel, H., Röttgers, R., Roy, S., Stramski, D., Thomalla, S., Platt, T., Sathyendranath, S., 2017. Validation and Intercomparison of Ocean Color Algorithms for Estimating Particulate Organic Carbon in the Oceans. Frontiers in Marine

Science 4.

Garcia Bravo, A., Bouchet, S., Amouroux, D., Poté, J., Dominik, J., 2011. Distribution of mercury and organic matter in particle-size classes in sediments contaminated by a waste water treatment plant: Vidy Bay, Lake Geneva, Switzerland. J Environ Monitor 13, 974-982.

Gordon, H.R., 1988. A semianalytic radiance model of ocean color. Journal of Geophysical Research 93, 10909-10924.

Gordon, H.R., 1997. Atmospheric correction of ocean color imagery in the Earth observing system era. Journal of Geophysical Research Atmospheres 102, 17081-17106.

Grunert, B.K., Mouw, C.B., Ciochetto, A.B., 2019. Deriving inherent optical properties from decomposition of hyperspectral non-water absorption. Remote Sens Environ 225, 193-206.

Guo, K., Zou, T., Jiang, D.J., Tang, C., Zhang, H., 2017. Variability of Yellow River turbid plume detected with satellite remote sensing during water-sediment regulation. Cont Shelf Res 135, 74-85.

Halse, G.R., Syvertsen, E.E., 1996. Chapter 2 - Marine Diatoms, in: Tomas, C.R. (Ed.), Identifying Marine Diatoms and Dinoflagellates. Academic Press, San Diego, pp. 5-385.

HOBI Laboratories, I., 2012. HydroScat-6 Spectral Backscattering Sensor USER'S MANUAL (Revision H).

Hovenier, M.I.M.J.W., 2000. Light Scattering by Nonspherical Particles: Theory, Measurements, and Applications. Meas Sci Technol 11, 1827-1827.

Hu, S., Zhang, L., Baig, M.H.A., Tong, Q., 2012. Using MODTRAN4 to build up a general look-up-table database for the atmospheric correction of hyperspectral imagery, International Geoscience and Remote Sensing Symposium (IGARSS), pp. 2458-2461.

Huang, C.C., Zhang, Y.L., Huang, T., Yang, H., Li, Y.M., Zhang, Z.G., He, M.Y., Hu, Z.J., Song, T., Zhu, A.X., 2019. Long-term variation of phytoplankton biomass and physiology in Taihu lake as observed via MODIS satellite. Water Res 153, 187-199.

Huang, C.C., Zou, J., Li, Y.M., Yang, H., Shi, K., Li, J.S., Wang, Y.H., Chena, X., Zheng, F., 2014. Assessment of NIR-red algorithms for observation of chlorophyll-a in highly turbid inland waters in China. Isprs J Photogramm 93, 29-39.

Huang, J., Chen, X.L., Jiang, T., Yang, F.L., Chen, L.Q., Yan, L.W., 2016. Variability of particle size distribution with respect to inherent optical properties in Poyang Lake, China. Appl Optics 55, 5821-5829.

Jonasz, M., Fournier, G.R., 2007. Light Scattering by Particles in Water: Theoretical and Experimental Foundations.

Jong, H.A., Grant, S.B., 2007. Size distribution, sources, and seasonality of suspended particles in southern California marine bathing waters. Environmental Science and Technology 41, 695-702.

Jorge, D.S.F., Barbosa, C.C.F., de Carvalho, L.A.S., Affonso, A.G., Lobo, F.L., Novo, E.L.M., 2017. SNR (signal-to-noise ratio) impact on water constituent retrieval from simulated images of optically complex Amazon lakes. Remote Sens-Basel 9.

Junge, C.E., 1963. Air chemistry and radioactivity. Academic press, New York.

Koestner, D., Stramski, D., Reynolds, R., 2019. Assessing the effects of particle size and composition on light scattering through measurements of size‐fractionated seawater samples. Limnol Oceanogr.

Kondolf, G.M., Schmitt, R.J.P., Carling, P., Darby, S., Arias, M., Bizzi, S., Castelletti, A., Cochrane, T.A., Gibson, S., Kummu, M., Oeurng, C., Zan, R.B., Wild, T., 2018. Changing

sediment budget of the Mekong: Cumulative threats and management strategies for a large river basin. Sci Total Environ 625, 114-134.

Kostadinov, T.S., Siegel, D.A., Maritorena, S., 2009. Retrieval of the particle size distribution from satellite ocean color observations. Journal of Geophysical Research Oceans 114, C09015.

Kostadinov, T.S., Siegel, D.A., Maritorena, S., Guillocheau, N., 2012. Optical assessment of particle size and composition in the Santa Barbara Channel, California. Appl Optics 51, 3171-3189.

Lamont, T., Brewin, R.J.W., Barlow, R.G., 2018. Seasonal variation in remotely-sensed phytoplankton size structure around southern Africa. Remote Sens Environ 204, 617-631.

Lee, Z., Carder, K.L., Mobley, C.D., Steward, R.G., Patch, J.S., 1998. Hyperspectral remote sensing for shallow waters. I. A semianalytical model. Appl Optics 37, 6329-6338.

Lei, S., Wu, D., Li, Y., Wang, Q., Huang, C., Liu, G., Zheng, Z., Du, C., Mu, M., Xu, J., Lyu, H., 2019a. Remote sensing monitoring of the suspended particle size in Hongze Lake based on GF-1 data. Int J Remote Sens 40, 3179-3203.

Lei, S., Xu, J., Li, Y., Du, C., Liu, G., Zheng, Z., Xu, Y., Lyu, H., Mu, M., Miao, S., Zeng, S., Xu, J., Li, L., 2020a. An approach for retrieval of horizontal and vertical distribution of total suspended matter concentration from GOCI data over Lake Hongze. Sci Total Environ 700, 134524.

Lei, S., Xu, J., Li, Y., Du, C., Mu, M., Zeng, S., Miao, S., Bi, S., Wang, Q., Lyu, H., 2019b. Remote Monitoring of PSD Slope Under the Influence of Sand Dredging Activities in Lake Hongze Based on Landsat-8/OLI Data and VIIRS/DNB Night-Time Light Composite Data. Ieee J-Stars 12, 4198 - 4212.

Lei, S., Xu, J., Li, Y., Lyu, H., Liu, G., Zheng, Z., Xu, Y., Du, C., Zeng, S., Wang, H., Dong, X., Cai, X., Li, J., 2020b. Temporal and spatial distribution of Kd(490) and its response to precipitation and wind in lake Hongze based on MODIS data. Ecol Indic 108, 105684.

Li, J., Chen, X., Tian, L., Huang, J., Feng, L., 2015. Improved capabilities of the Chinese high-resolution remote sensing satellite GF-1 for monitoring suspended particulate matter (SPM) in inland waters: Radiometric and spatial considerations. Isprs J Photogramm 106, 145-156.

Li, J., Ma, R., Xue, K., Zhang, Y., Loiselle, S., 2018. A Remote Sensing Algorithm of Column-Integrated Algal Biomass Covering Algal Bloom Conditions in a Shallow Eutrophic Lake. Isprs Int Geo-Inf 7, 466.

Li, J., Tian, L., Song, Q., Huang, J., Li, W., Wei, A., 2019a. A Near-Infrared Band-Based Algorithm for Suspended Sediment Estimation for Turbid Waters Using the Experimental Tiangong 2 Moderate Resolution Wide-Wavelength Imager. Ieee J-Stars 12, 774-787.

Li, J.W., Yu, Q., Tian, Y.Q., Becker, B.L., 2017. Remote sensing estimation of colored dissolved organic matter (CDOM) in optically shallow waters. Isprs J Photogramm 128, 98-110.

Li, N., Shi, K., Zhang, Y., Gong, Z., Peng, K., Zhang, Y., Zha, Y., 2019b. Decline in Transparency of Lake Hongze from Long-Term MODIS Observations: Possible Causes and Potential Significance. Remote Sens-Basel 11, 177.

Lin, J.F., Lee, Z.P., Ondrusek, M., Liu, X.H., 2018. Hyperspectral absorption and backscattering coefficients of bulk water retrieved from a combination of remote-sensing reflectance and attenuation coefficient. Opt Express 26, A157-A177.

Liu, G., Li, L., Song, K., Li, Y., Lyu, H., Wen, Z., Fang, C., Bi, S., Sun, X., Wang, Z., Cao, Z.,

Shang, Y., Yu, G., Zheng, Z., Huang, C., Xu, Y., Shi, K., 2020. An OLCI-based algorithm for semi-empirically partitioning absorption coefficient and estimating chlorophyll a concentration in various turbid case-2 waters. Remote Sens Environ 239, 111648.

Loisel, H., Nicolas, J.M., Sciandra, A., Stramski, D., Poteau, A., 2006. Spectral dependency of optical backscattering by marine particles from satellite remote sensing of the global ocean. Journal of Geophysical Research: Oceans 111.

Lyu, H., Wang, Y.N., Jin, Q., Shi, L., Li, Y.M., Wang, Q., 2017. Developing a semi-analytical algorithm to estimate particulate organic carbon (POC) levels in inland eutrophic turbid water based on MERIS images: A case study of Lake Taihu. Int J Appl Earth Obs 62, 69-77.

Maeda, E.E., Lisboa, F., Kaikkonen, L., Kallio, K., Koponen, S., Brotas, V., Kuikka, S., 2019. Temporal patterns of phytoplankton phenology across high latitude lakes unveiled by long-term time series of satellite data. Remote Sens Environ 221, 609-620.

Maffione, R.A., Dana, D.R., 1997. Instruments and methods for measuring the backward-scattering coefficient of ocean waters. Appl Optics 36, 6057-6067.

Mendes, R., Saldias, G.S., deCastro, M., Gomez-Gesteira, M., Vaz, N., Dias, J.M., 2017. Seasonal and interannual variability of the Douro turbid river plume, northwestern Iberian Peninsula. Remote Sens Environ 194, 401-411.

Miao, S., Lyu, H., Wang, Q., Li, Y.M., Wu, Z.M., Du, C.G., Xu, J., Bi, S., Mu, M., Lei, S.H., 2019. Estimation of terrestrial humic-like substances in inland lakes based on the optical and fluorescence characteristics of chromophoric dissolved organic matter (CDOM) using OLCI images. Ecol Indic 101, 399-409.

Mie, G., 1908. Beiträge zur Optik trüber Medien, speziell kolloidaler Metallösungen. Annalen der Physik 330, 377-445.

Minghelli, A., Lei, M., Charmasson, S., Rey, V., Chami, M., 2019. Monitoring Suspended Particle Matter Using GOCI Satellite Data After the Tohoku (Japan) Tsunami in 2011. Ieee J-Stars 12, 567-576.

Mishra, D.R., Narumalani, S., Rundquist, D., Lawson, M., 2005. Characterizing the vertical diffuse attenuation coefficient for downwelling irradiance in coastal waters: Implications for water penetration by high resolution satellite data. Isprs J Photogramm 60, 48-64.

Mu, M., Wu, C., Li, Y., Lyu, H., Fang, S., Yan, X., Liu, G., Zheng, Z., Du, C., Bi, S., 2019. Long-term observation of cyanobacteria blooms using multi-source satellite images: a case study on a cloudy and rainy lake. Environ Sci Pollut R 26, 11012-11028.

Mueller, J.L., Morel, A., Frouin, R., Davis, C., Arnone, R., Carder, K., Lee, Z.P., 2003. Ocean optics protocols for satellite ocean color sensor validation, revision 4, volume III: Radiometric Measurements and Data Analysis Protocols. NASA Tech. Memo., 21-31.

Neukermans, G., Loisel, H., Meriaux, X., Astoreca, R., Mckee, D., 2012. In situ variability of mass-specific beam attenuation and backscattering of marine particles with respect to particle size, density, and composition. Limnol Oceanogr 57, 124-144.

Ogashawara, I., Mishra, D.R., Nascimento, R.F.F., Alcântara, E.H., Kampel, M., Stech, J.L., 2016. Re-parameterization of a quasi-analytical algorithm for colored dissolved organic matter dominant inland waters. Int J Appl Earth Obs 53, 128-145.

Organelli, E., Dall'Olmo, G., Brewin, R.J.W., Tarran, G.A., Boss, E., Bricaud, A., 2018. The open-ocean missing backscattering is in the structural complexity of particles. Nat Commun 9.

Oyama, Y., Matsushita, B., Fukushima, T., Matsushige, K., Imai, A., 2009. Application of

spectral decomposition algorithm for mapping water quality in a turbid lake (Lake Kasumigaura, Japan) from Landsat TM data. Isprs J Photogramm 64, 73-85.

Peng, F., Effler, S.W., 2012. Mass-specific scattering coefficient for natural minerogenic particle populations: Particle size distribution effect and closure analyses. Appl Optics 51, 2236-2249.

Peng, K., Cai, Y.J., Qin, B.Q., Gong, Z.J., 2019. The effect of wind speed decline on macroinvertebrates in Lake Taihu, China. Sci Total Environ 662, 481-489.

Pope, R.M., Fry, E.S., 1997. Absorption spectrum (380-700 nm) of pure water. II. Integrating cavity measurements. Appl Optics 36, 8710-8723.

Qi, L., Hu, C.M., Visser, P.M., Ma, R.H., 2018. Diurnal changes of cyanobacteria blooms in Taihu Lake as derived from GOCI observations. Limnol Oceanogr 63, 1711-1726.

Qing, S., Zhang, J., Cui, T., Bao, Y., 2014. Remote sensing retrieval of inorganic suspended particle size in the Bohai Sea. Cont Shelf Res 73, 64-71.

Reynolds, R., Stramski, D., 2019. Optical characterization of marine phytoplankton assemblages within surface waters of the western Arctic Ocean. Limnol Oceanogr.

Reynolds, R., Stramski, D., Neukermans, G., 2016. Optical backscattering by particles in Arctic seawater and relationships to particle mass concentration, size distribution, and bulk composition. Limnol Oceanogr 61, 1869–1890.

Reynolds, R.A., Stramski, D., Wright, V.M., Woźniak, S.B., 2010. Measurements and characterization of particle size distributions in coastal waters. Journal of Geophysical Research Oceans 115, C08024.

Risović, D., 2002. Effect of suspended particulate-size distribution on the backscattering ratio in the remote sensing of seawater. Appl Optics 41, 7092-7101.

Ruddick, K.G., Ovidio, F., Rijkeboer, M., 2000. Atmospheric correction of SeaWiFS imagery for turbid coastal and inland waters. Appl Optics 39, 897-912.

Serra, T., Colomer, J., Cristina, X.P., Vila, X., Arellano, J.B., Casamitjana, X., 2001. Evaluation of laser in situ scattering instrument for measuring concentration of phytoplankton, purple sulfur bacteria, and suspended inorganic sediments in lakes. Journal of Environmental Engineering 127, 1023-1030.

Sheldon, R.W., Prakash, A., Sutcliffe, W.H., Jr., 1972. THE SIZE DISTRIBUTION OF PARTICLES IN THE OCEAN. Limnol Oceanogr 17, 327-340.

Shi, K., Zhang, Y., Song, K., Liu, M., Zhou, Y., Zhang, Y., Li, Y., Zhu, G., Qin, B., 2019a. A semi-analytical approach for remote sensing of trophic state in inland waters: Bio-optical mechanism and application. Remote Sens Environ 232, 111349.

Shi, K., Zhang, Y., Zhu, G., Liu, X., Zhou, Y., Xu, H., Qin, B., Liu, G., Li, Y., 2015. Long-term remote monitoring of total suspended matter concentration in Lake Taihu using 250 m MODIS-Aqua data. Remote Sens Environ 164, 43-56.

Shi, W., Wang, M., 2019. Characterization of Suspended Particle Size Distribution in Global Highly Turbid Waters From VIIRS Measurements. Journal of Geophysical Research: Oceans 124, 3796-3817.

Shi, W., Wang, M.H., Zhang, Y.L., 2019b. Inherent Optical Properties in Lake Taihu Derived from VIIRS Satellite Observations. Remote Sens-Basel 11.

Shi, W., Zhang, Y.L., Wang, M.H., 2018. Deriving Total Suspended Matter Concentration from the Near-Infrared-Based Inherent Optical Properties over Turbid Waters: A Case Study in Lake Taihu. Remote Sens-Basel 10.

Song, K.S., Ma, J.H., Wen, Z.D., Fang, C., Shang, Y.X., Zhao, Y., Wang, M., Du, J., 2017. Remote estimation of K-d (PAR) using MODIS and Landsat imagery for turbid inland

waters in Northeast China. Isprs J Photogramm 123, 159-172.

Stramski, D., 1999. Refractive index of planktonic cells as a measure of cellular carbon and chlorophyll a content. Deep-Sea Research Part I: Oceanographic Research Papers 46, 335-351.

Stramski, D., Boss, E., Bogucki, D., Voss, K.J., 2004. The role of seawater constituents in light backscattering in the ocean. Prog Oceanogr 61, 27-56.

Stramski, D., Kiefer, D.A., 1991. Light scattering by microorganisms in the open ocean. Prog Oceanogr 28, 343-383.

Stramski, D., Mobley, C.D., 1997. Effects of microbial particles on oceanic optics: A database of single-particle optical properties. Limnol Oceanogr 42, 538-549.

Sun, D., Lai, W., Wang, S., Huan, Y., Bilal, M., Qiu, Z., He, Y., 2019. Synoptic relationships to estimate phytoplankton communities specific to sizes and species from satellite observations in coastal waters. Opt Express 27, A1156-A1172.

Sun, D., Qiu, Z., Hu, C., Wang, S., Wang, L., Zheng, L., Peng, T., He, Y., 2016. A hybrid method to estimate suspended particle sizes from satellite measurements over Bohai Sea and Yellow Sea. Journal of Geophysical Research Oceans 121, 6742-6761.

Sun, D.Y., Huan, Y., Qiu, Z.F., Hu, C.M., Wang, S.Q., He, Y.J., 2017. Remote-Sensing Estimation of Phytoplankton Size Classes From GOCI Satellite Measurements in Bohai Sea and Yellow Sea. Journal of Geophysical Research Oceans 122, 8309-8325.

Tamigneaux, E., Legendre, L., Klein, B., Mingelbier, M., 1999. Seasonal dynamics and potential fate of size-fractionated phytoplankton in a temperate nearshore environment (western Gulf of St Lawrence, Canada). Estuarine, Coastal and Shelf Science 48, 253-269.

Tang, J., 2007. The Species Composition,Abundance and Distribution in Habitat of Geese and Ducks in the Eastern Hongzehu Wetland Natural Reserve. Chinese Journal of Zoology 42, 94-101.

Thorne, P.D., Hurther, D., 2014. An overview on the use of backscattered sound for measuring suspended particle size and concentration profiles in non-cohesive inorganic sediment transport studies. Cont Shelf Res 73, 97-118.

Thosteson, E.D., Hanes, D.M., 1998. A simplified method for determining sediment size and concentration from multiple frequency acoustic backscatter measurements. The Journal of the Acoustical Society of America 104, 820-830.

Vaillancourt, R.D., Brown, C.W., Guillard, R.R.L., Balch, W.M., 2004. Light backscattering properties of marine phytoplankton: relationships to cell size, chemical composition and taxonomy. Journal of Plankton Research 26, 191-212.

Villa, P., Pinardi, M., Bolpagni, R., Gillier, J.-M., Zinke, P., Nedelcuţ, F., Bresciani, M., 2018. Assessing macrophyte seasonal dynamics using dense time series of medium resolution satellite data. Remote Sens Environ 216, 230-244.

Wang, M.Q., Hu, C.M., Barnes, B.B., Mitchum, G., Lapointe, B., Montoya, J.P., 2019. The great Atlantic Sargassum belt. Science 365, 83-+.

Wang, S.Q., Qiu, Z.F., Sun, D.Y., Shen, X.J., Zhang, H.L., 2016. Light beam attenuation and backscattering properties of particles in the Bohai Sea and Yellow Sea with relation to biogeochemical properties. J Geophys Res-Oceans 121, 3955-3969.

Watanabe, F., Alcantara, E., Imai, N., Rodrigues, T., Bernardo, N., 2018. Estimation of Chlorophyll-a Concentration from Optimizing a Semi-Analytical Algorithm in Productive Inland Waters. Remote Sens-Basel 10.

Watanabe, F., Mishra, D.R., Astuti, I., Rodrigues, T., Alcantara, E., Imai, N.N., Barbosa, C., 2016. Parametrization and calibration of a quasi-analytical algorithm for tropical

eutrophic waters. Isprs J Photogramm 121, 28-47.

Wedd, M., Ward-Smith, S., Rawle, A., 2019. Particle Size Analysis☆, in: Worsfold, P., Poole, C., Townshend, A., Miró, M. (Eds.), Encyclopedia of Analytical Science (Third Edition). Academic Press, Oxford, pp. 144-157.

Welschmeyer, N.A., 1994. Fluorometric analysis of chlorophyll a in the presence of chlorophyll b and pheopigments. Limnol Oceanogr 39, 1985-1992.

Werdell, P.J., McKinna, L.I.W., Boss, E., Ackleson, S.G., Craig, S.E., Gregg, W.W., Lee, Z., Maritorena, S., Roesler, C.S., Rousseaux, C.S., Stramski, D., Sullivan, J.M., Twardowski, M.S., Tzortziou, M., Zhang, X., 2018. An overview of approaches and challenges for retrieving marine inherent optical properties from ocean color remote sensing. Prog Oceanogr 160, 186-212.

Wozniak, S.B., Sagan, S., Zablocka, M., Ston-Egiert, J., Borzycka, K., 2018. Light scattering and backscattering by particles suspended in the Baltic Sea in relation to the mass concentration of particles and the proportions of their organic and inorganic fractions. J Marine Syst 182, 79-96.

Wu, G., Cui, L., Duan, H., Fei, T., Liu, Y., 2011. Absorption and backscattering coefficients and their relations to water constituents of Poyang Lake, China. Appl Optics 50, 6358-6368.

Xi, H., Larouche, P., Tang, S., Michel, C., 2014. Characterization and variability of particle size distributions in Hudson Bay, Canada. Journal of Geophysical Research Oceans 119, 3392-3406.

Xiong, J., Lin, C., Ma, R., Cao, Z., 2019. Remote Sensing Estimation of Lake Total Phosphorus Concentration Based on MODIS: A Case Study of Lake Hongze. Remote Sens-Basel 11.

Xu, J., Fang, C.Y., Gao, D., Zhang, H.S., Gao, C., Xu, Z.C., Wang, Y.Q., 2018. Optical models for remote sensing of chromophoric dissolved organic matter (CDOM) absorption in Poyang Lake. Isprs J Photogramm 142, 124-136.

Xu, J., Lei, S., Bi, S., Li, Y., Lyu, H., Xu, J., Xu, X., Mu, M., Miao, S., Zeng, S., Zheng, Z., 2019a. Tracking spatio-temporal dynamics of POC sources in eutrophic lakes by remote sensing. Water Res, 115162.

Xu, J., Lyu, H., Xu, X., Li, Y., Li, Z., Lei, S., Bi, S., Mu, M., Du, C., Zeng, S., 2019b. Dual stable isotope tracing the source and composition of POM during algae blooms in a large and shallow eutrophic lake: All contributions from algae? Ecol Indic 102, 599-607.

Xu, Y., Qin, B., Zhu, G., Zhang, Y., Shi, K., Li, Y., Shi, Y., Chen, L., 2019c. High Temporal Resolution Monitoring of Suspended Matter Changes from GOCI Measurements in Lake Taihu. Remote Sens-Basel 11, 985.

Xue, K., Ma, R., Duan, H., Shen, M., Boss, E., Cao, Z., 2019. Inversion of inherent optical properties in optically complex waters using sentinel-3A/OLCI images: A case study using China's three largest freshwater lakes. Remote Sens Environ 225, 328-346.

Yu, X., 2019. Impacts of pure seawater absorption coefficient on remotely sensed inherent optical properties in oligotrophic waters. Opt Express 27, 34974.

Zeng, S., Lei, S., Li, Y., Lyu, H., Xu, J., Dong, X., Wang, R., Yang, Z., Li, J., 2020. Retrieval of Secchi Disk Depth in Turbid Lakes from GOCI Based on a New Semi-analytical Algorithm. Remote Sens-Basel 12.

Zhang, F.F., Li, J.S., Shen, Q., Zhang, B., Tian, L.Q., Ye, H.P., Wang, S.L., Le, Z.Y., 2019a. A soft-classification-based chlorophyll-a estimation method using MERIS data in the highly turbid and eutrophic Taihu Lake. Int J Appl Earth Obs 74, 138-149.

Zhang, M., Tang, J., Song, Q., Dong, Q., 2010. Backscattering ratio variation and its implications for studying particle composition: A case study in Yellow and East China seas. Journal of Geophysical Research: Oceans 115.

Zhang, Y., Liang, J., Zeng, G., Tang, W., Lu, Y., Luo, Y., Xing, W., Tang, N., Ye, S., Li, X., Huang, W., 2019b. How climate change and eutrophication interact with microplastic pollution and sediment resuspension in shallow lakes: A review. Sci Total Environ, 135979.

Zhang, Y.L., Shi, K., Zhou, Y.Q., Liu, X.H., Qin, B.Q., 2016. Monitoring the river plume induced by heavy rainfall events in large, shallow, Lake Taihu using MODIS 250 m imagery. Remote Sens Environ 173, 109-121.

Zhang, Y.L., Zhang, B., Wang, X., Li, J.S., Feng, S., Zhao, Q.H., Liu, M.L., Qin, B.Q., 2007. A study of absorption characteristics of chromophoric dissolved organic matter and particles in Lake Taihu, China. Hydrobiologia 592, 105-120.

Zhao, W., Sun, L., Cui, T., Cao, W., Ma, Y., Hao, Y., 2014. Mapping the distribution of suspended particulate matter concentrations influenced by storm surge in the Yellow River Estuary using FY-3A MERSI 250-m data. Aquat Ecosyst Health 17, 290-298.

Zuo, Q., Chen, Y., Jie, T., 2012. Climate Change and its Impact on Water Resources in the Huai River Basin. Bulletin of the Chinese Academy of Sciences 26, 32-39.